nature physics

Article

https://doi.org/10.1038/s41567-025-02870-4

Impact of impurities on crystal growth

Received: 8 August 2024

Accepted: 7 March 2025

Published online: 15 April 2025

Check for updates

Qiong Gao[1,5], Huang Fang[1,5], Dong Xiang[1], Yanshuang Chen[1], Hajime Tanaka[2,3] ✉ & Peng Tan[1,4] ✉

Impurities critically influence crystallization, a process fundamental to both physical sciences and industrial engineering. However, understanding how impurity transport affects crystallization presents substantial experimental challenges. Here we visualized crystallization at the single-particle level for a relatively high concentration of impurities. We observed a bifurcation in growth modes—continuous growth or melting and recrystallization—governed by the ability of the system to remove impurity particles from the growth front. The initial nucleation configuration determines the crystal grain size and growth-front morphology, which in turn influence impurity transport. Small grains promote lateral impurity transport to grain boundaries, thus reducing impurity concentration and favouring continuous growth, whereas larger grains accumulate impurities, leading to melting and recrystallization. We reveal that the latter arises from the competition between crystallization and vitrification, which is a form of devitrification. This study provides insights into the relation between impurity concentration and crystallization pathways and highlights how the initial configuration shapes the final crystal morphology.

Crystallization is the process by which randomly arranged particles (atoms or molecules) in a liquid spontaneously organize into a long-range-ordered periodic structure. This process is fundamental in creating the microstructure and mechanical properties of polycrystalline materials, including metals, alloys and ceramics[1–7]. Crystallization proceeds through nucleation and growth. Initially, small nuclei form[8–13], and these subsequently expand as their growth front advances[14–19]. The kinetics at the growth front are critical in shaping the ultimate morphology of the crystal. Factors such as the microscale roughness and orientation of the growth front heavily influence the rates of particle attachment and detachment, which, in turn, determine the overall crystal growth rate[20–22]. Instabilities at the growth front, which are driven by a mechanical imbalance, can result in the formation of intricate anisotropic patterns like dendritic arrays[23–27] or may facilitate rapid glass-to-crystal transitions at ultra-low temperatures[28–31].

Impurities, often referred to as 'foreign particles', are present during most natural crystallization processes. They influence the phase behaviour and crystallization pathway of host particles based on their size, shape, concentration and interactions with the host particles[1]. Foreign particles can either accelerate or hinder crystallization: they can lower the nucleation barrier to promote faster crystallization[32], slow it down by reducing the host particle mobility and introducing defects[33], or initially accelerate and then decelerate growth[34]. Additionally, they can disrupt the mechanical stability of the growth front, leading to enhanced anisotropy in the crystal morphology[35–37].

By exploiting these effects, material scientists have harnessed foreign particles to control crystallization, thus facilitating the design and development of unique and functional materials. These approaches have found widespread applications in diverse fields, including rainmaking[38], semiconductor doping[39,40], metal alloy production[41,42] and polymer crystallization[43].

Despite extensive studies, the microscopic mechanisms by which foreign particles influence crystallization remain elusive, particularly at high foreign-particle concentrations. Most existing research has focused on dilute conditions, where foreign particles are sparse relative to host particles. In these cases, they interact minimally with

[1]Department of Physics and State Key Laboratory of Surface Physics, Fudan University, Shanghai, P. R. China. [2]Research Center for Advanced Science and Technology, The University of Tokyo, Tokyo, Japan. [3]Department of Fundamental Engineering, Institute of Industrial Science, The University of Tokyo, Tokyo, Japan. [4]Institute for Nanoelectronic Devices and Quantum Computing, Fudan University, Shanghai, P. R. China. [5]These authors contributed equally: Qiong Gao, Huang Fang. ✉e-mail: tanaka@iis.u-tokyo.ac.jp; tanpeng@fudan.edu.cn

one another and primarily form isolated point defects within the crystal structure. Theories such as those proposed by Cabrera and Vermilyea[44], combined with phase-field computations[45–47], have effectively described how foreign particles interact with substructures (for example, terraces, steps and kinks[48]) at the crystal growth front. This approach treats foreign particles as static, independent sources of frustration. However, when the foreign-particle concentration surpasses a critical threshold, crystallization is increasingly suppressed, leading to vitrification under deep supercooling[49,50]. Near this threshold, frequent interactions among foreign particles result in highly complex and unpredictable defect behaviours. This regime remains largely unexplored, both experimentally and theoretically, leaving fundamental questions unanswered. How does the growth front behave in the presence of numerous foreign particles? How do these changes affect the final crystal morphology? These gaps in understanding highlight the need for further experimental and theoretical exploration of high-concentration impurity regimes.

In this study, we explored how the initial configuration of crystal nuclei influences subsequent growth pathways in the presence of a relatively high concentration of foreign particles. By selecting colloidal particles with a suitable size and Brownian time (the characteristic timescale for particle diffusion), we successfully captured the long-term three-dimensional (3D) crystal growth process at the single-particle level using confocal microscopy. A detailed analysis of the growth dynamics allowed us to explore the competition and interplay between growing crystalline grains and surrounding liquid melts at the growth front. We identified two distinct growth modes under identical experimental conditions: stable continuous growth (CG) and unstable growth involving repetitive melting and recrystallization (MR). The bifurcation between these modes was driven by the competition between crystallization and vitrification. Further analysis revealed that variations in the initial distribution of nuclei strongly affected the growth pathway, with changes in nucleation configuration either promoting impurity transport to grain boundaries (favouring CG) or leading to impurity accumulation at the growth front (triggering MR).

Results and discussion

Experiment

Our system consisted of a binary charged colloidal suspension of large (radius $\sigma_l = 2.10 \pm 0.05$ μm) and small (radius $\sigma_s = 1.06 \pm 0.02$ μm) poly(methyl methacrylate) particles dispersed in a non-polar organic solvent mixture containing hexachloro-1,3-butadiene, tetrachloroethylene and decahydronaphthalene. The small particles acted as foreign particles, with their fraction relative to the total number of particles N_s/N serving as a key control parameter, where N_s represents the number of foreign particles and N the total particle count. This fraction was varied between 10% and 25%. As the small particles were composed of the same material as the large ones and were present in a relatively high proportion, the system can be considered a binary mixture. In this context, referring to the small particles as 'impurities' may be somewhat misleading. However, we chose to use this terminology because, during the crystallization of the larger particles, the small particles effectively function as impurities or foreign elements.

Another critical control parameter was the concentration of the surfactant sodium di-2-ethylhexyl sulfosuccinate (AOT), C_{AOT}, which formed charged micelles to regulate the Debye length (κ^{-1}) governing the screened electrostatic interaction between particles. C_{AOT} was tuned between 10 and 50 mM. The total volume fraction of particles was maintained at 20%. In the absence of foreign particles, both body-centred cubic (BCC) and face-centred cubic (FCC) crystal structures formed at this volume fraction (Fig. 1a, top). When $C_{AOT} \gtrsim 12$ mM ($\kappa\sigma_l \gtrsim 3$), the system had an FCC structure, whereas for $C_{AOT} \lesssim 12$ mM ($\kappa\sigma_l \lesssim 3$), BCC crystals were observed.

Both large and small particles were fluorescently labelled with nitrobenzoxadiazole and grafted with polyhydroxystearic acid polymer to prevent coagulation. The colloidal particles were density- and refractive-index-matched to the solvent to minimize gravitational and optical distortion. The sample was sealed in a glass capillary with dimensions of 100 μm × 100 μm × 100 μm. To prevent particle adhesion, the inner wall of the capillary was pretreated with the same solvent as the suspension. Before starting observations, while sealing the sample, we shear-melted any pre-existing crystal structures by magnetically stirring nickel powder inside the chamber. The system was then left at room temperature and monitored using confocal microscopy (Leica SP8 Fast) for over 13 h. Time-lapse 3D images were captured every 14 min with a z-direction scanning speed of approximately 3.5 μm s^{-1}, which allowed us to track the crystallization pathways and morphological evolution at single-particle resolution.

The bifurcation of crystal growth modes

Two distinct crystal growth modes were observed in the experimental parameter space. One mode, the CG mode, is characterized by uninterrupted crystal growth throughout the crystallization process. The other mode, the MR mode, involves transient local melting of the crystal followed by subsequent growth, resulting in intermittent growth. The phase diagram with foreign particles, shown in Fig. 1a (bottom), shows the distribution of these growth modes. At low foreign-particle fractions ($N_s/N \lesssim 12\%$, G's), only the CG mode was observed. As the foreign-particle fraction was increased, the crystal growth rate decreased (see Methods for the calculation details). The MR mode began to emerge and coexist with the CG mode at $N_s/N \approx 15\%$ (Y's). The ratio of CG to MR modes in this region was approximately 7:3. Notably, the emergence of the MR mode was independent of the lattice structure formed by the large particles, as it was observed in both BCC and FCC structures. As N_s/N or C_{AOT} was increased further, a glassy structure formed (X's). Interestingly, a rare avalanche-like crystallization event was observed deep within the glass phase region, which was characterized by sudden and rapid crystal growth that terminated almost immediately (L).

In the CG mode, the crystal growth front advanced continuously in three dimensions (Supplementary Video 1). Figure 1b has cross-sectional views of five crystal grains at a height of $z \approx 2d$ ($d = 2.2$ μm is the interlayer spacing of the (110) face of the BCC lattice). The orientation of each grain is represented by its colour. These grains grew laterally in both the x and y directions until their boundaries came into contact. Simultaneously, the average grain size L and the characteristic height $\langle h \rangle$ increased monotonically, as shown in Fig. 1d (see Methods for the calculation details). The spatial distribution of crystalline order also evolved, further demonstrating the CG of the crystalline domain. Figure 1f depicts the temporal evolution of $\langle \overline{q_6} \rangle$ as a function of z, where $\langle q_6 \rangle$ is the coarse-grained Steinhardt local bond orientational order parameter used to quantify the local crystalline order[51]. Here, $\langle \overline{q_6} \rangle$ represents the average q_6 of all the particles within a thin layer with thickness equal to d at various z values (see Methods for the calculation details). Higher values of $\langle \overline{q_6} \rangle$ correspond to a larger fraction of particles in the crystalline state at that height z. The continuous rise and advance of the $\langle \overline{q_6} \rangle$ profile clearly demonstrate the expansion of the crystalline domain in both the lateral and vertical directions.

By contrast, in the MR mode, the crystal growth front experienced several instances of local melting and recrystallization, characterized by pronounced shrinkage and re-expansion of the crystalline domain. As shown in Fig. 1c, the grain size decreased in the lateral direction after a local melting event and was accompanied by an approximately 10° change in its orientation. Figure 1e displays two sudden drops in the average grain size L and the characteristic height $\langle h \rangle$ within the experimental observation time, corresponding to these local melting events. These events are also reflected in the temporal evolution of the system order. After a local melting event, the $\langle \overline{q_6} \rangle$ profile exhibited an overall downward shift compared to its position before melting (Fig. 1g), indicating the shrinkage of the crystalline domain in all three

https://doi.org/10.1038/s41567-025-02870-4

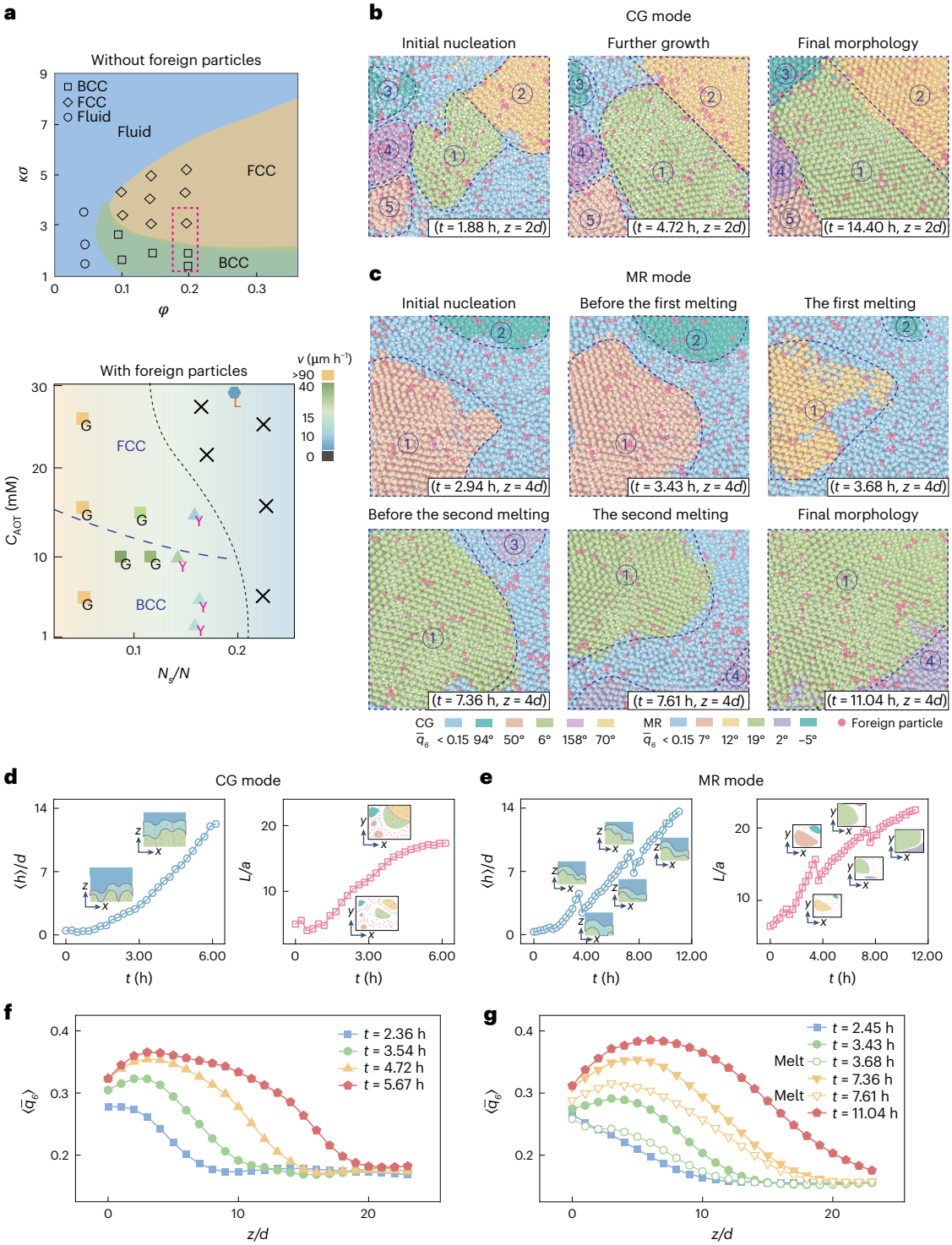

Fig. 1 | Two growth modes. a, Top, phase diagram of a monodisperse charged colloidal system, plotted as a function of the volume fraction (φ) and the inverse Debye length ($\kappa\sigma$). Different symbols indicate various phases. Circles represent fluid, rhombuses indicate FCC and squares denote BCC. Bottom, dynamic phase diagram of the experimental system with foreign particles, shown as a function of AOT concentration (C_{AOT}) and foreign-particle fraction (N_s/N). G's represent CG, Y's denote the coexistence of two growth modes, L indicates local crystal growth and X's denote glass formation. The dark blue dashed and black dotted lines mark the FCC–BCC boundary and the crystal–glass boundary, respectively. Symbol colours correspond to CG speeds. **b**,**c**, Cross-sectional views of the grain-morphology evolution at a fixed height z in terms of the interlayer spacing d for the CG mode (**b**) and the MR mode (**c**), with grains colour-coded by orientation. Pink spheres represent foreign particles. **d**,**e**, Characteristic height $\langle h \rangle$ (left panel) and average grain size L (right panel) as functions of time for the CG mode (**d**) and the MR mode (**e**). Insets, schematics of the morphologies in the x–y and x–z planes. **f**,**g**, Evolution of the average order parameter profile $\langle \overline{q_6} \rangle$ as a function of z for the CG mode (**f**) and the MR mode (**g**).

https://doi.org/10.1038/s41567-025-02870-4

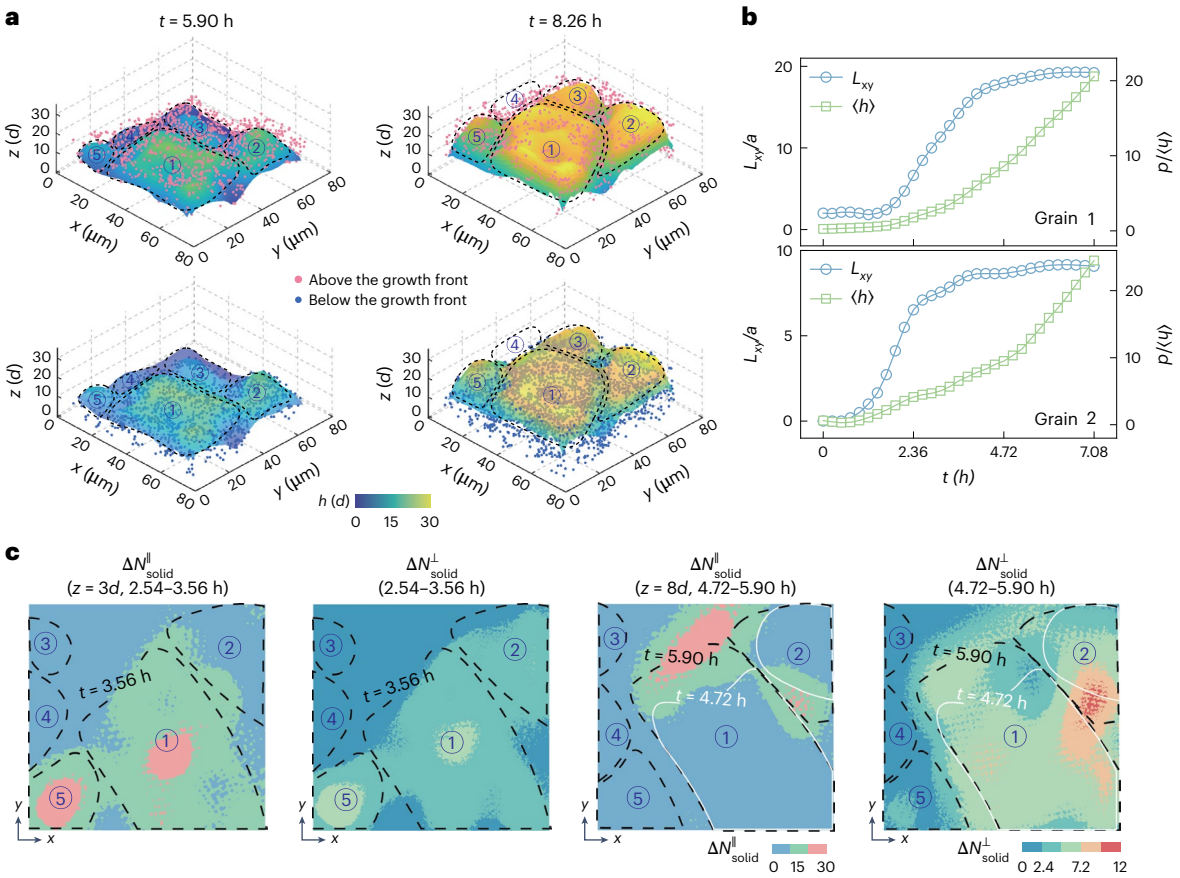

Fig. 2 | The kinetic pathway of the CG mode. a, Evolution of growth-front morphology and foreign-particle distribution. Top, foreign particles (pink spheres) within the four layers above the growth front. Bottom, their distribution (blue spheres) within the grains. The colour bar represents the local height of the solid. **b**, Temporal evolution of grain size in the lateral direction (L_{xy}) and vertical direction ($\langle h \rangle$). Here, a represents the interparticle spacing in the solid, and d corresponds to the interlayer spacing of the (100) face in the BCC crystal lattice. **c**, Temporal evolution of the local change in the number of solid particles $\Delta N^{\parallel}_{solid}(x,y,z)$ at a fixed height z and its integration along the z axis, $\Delta N^{\perp}_{solid}(x,y)$. $\Delta N^{\parallel}_{solid}(x,y,z)$ quantifies changes in the number of solid particles within a finite cylindrical volume of radius $3a$ and height d centred at (x,y,z). $\Delta N^{\perp}_{solid}(x,y)$ characterizes changes within an infinitely tall cylindrical volume of radius $3a$ centred at (x,y) and representing vertical growth or melting. The white and black dashed lines indicate the initial and final positions of the growth front during the observed time interval.

dimensions. Notably, the overall $\langle \overline{q_6} \rangle$ values remained relatively high because the cores of the large crystalline domains remained in the solid state. Melting occurred only locally at their growth front rather than in the bulk of the crystal.

Interestingly, these two modes exhibited different initial nuclei configurations and final crystal morphologies. The initial number density of crystal nuclei predetermined the size limit of the crystalline grains, which, in turn, influenced the accommodation capacity for foreign particles. Smaller grains have a greater surface area for accommodating foreign particles, some of which become inclusions within the grains, while others segregate at the grain boundaries. In the CG mode, as shown in Extended Data Fig. 1a, the system initially contained five crystal nuclei, and the grain size remained relatively small. Owing to the limited accommodation for foreign particles within the grains, most of the foreign particles were transported to the grain boundaries. This resulted in a final system that remained polycrystalline being composed of five grains.

Conversely, in the MR mode, as depicted in Extended Data Fig. 1b, the system initially contained one large and one small grain. The maximum size of a grain was larger than in the CG mode. Only the grain interiors and a few grain boundary areas could accommodate foreign particles. As a result, the system ultimately formed one large grain and one small grain. Further analysis of the uniformity of the foreign-particle distribution (Extended Data Fig. 1c) revealed that the emergence of MR modes was typically associated with a less uniform initial arrangement of foreign particles. This spatial heterogeneity in the foreign-particle distribution seems to be linked to the non-uniformity of the initial nuclei distribution. This effect was particularly pronounced near the crystal–glass boundary, where the slow diffusion of foreign particles impeded the relaxation of their non-uniform distribution, thereby increasing the likelihood of a MR mode occurring.

The kinetic pathway of the CG mode

Next, we elaborate on the kinetic pathway of crystal growth in the two growth modes from a microscopic perspective. We found that the morphology of the growth front and grain size play crucial roles in determining the crystal growth process. Both factors substantially influenced the transport behaviour of foreign particles during crystal growth. The shape and dynamics of the growth front dictated how foreign particles were incorporated into the growing crystals, whereas the grain size affected the capacity of the crystals to accommodate these particles, ultimately shaping the final microstructure.

In the CG mode, the growth front was highly rugged and expanded anisotropically in 3D space. As depicted in Fig. 2a and Supplementary Video 1, the system initially contained five nuclei. As the nuclei grew, the crystal growth front exhibited a rugged morphology, with peaks formed by the crystalline regions and valleys formed by the liquid

regions. As the crystals grew, they could trap foreign particles within their grains as interstitial atoms or defects (Extended Data Fig. 2), and the capacity of the grains to trap these particles was directly proportional to their size. When the number of foreign particles exceeded the trapping capacity of the grains, the advantages of the rugged growth-front morphology enabled the foreign particles to laterally diffuse to the grain boundaries or vertically diffuse into the liquid region above the crystal. This dynamic process substantially influenced the final distribution of foreign particles within the system.

Figure 2b shows the evolution of the crystalline domain size in the lateral (L_{xy}) and vertical ($\langle h \rangle$) directions (see Methods for the calculation details). Initially, L_{xy} grew fast before plateauing, whereas $\langle h \rangle$ grew slowly at first and then accelerated. Figure 2c provides a direct comparison of the advance of the growth front in the lateral and vertical directions by illustrating the distribution of the local change in the number of solid particles $\Delta N^{\parallel}_{\mathrm{solid}}$ and their integration along the z direction $\Delta N^{\perp}_{\mathrm{solid}}$ (see Methods for the calculation details). During the initial period (2.54 h < t < 3.56 h), new grains (for example, grains 1 and 5) nucleated and grew in all three dimensions, with relatively faster growth in the lateral direction. As the grains started to touch each other (4.72 h < t < 5.90 h), the lateral growth was suppressed. Only grain 1 continued to expand slightly in the +y direction due to the availability of free space, while vertical growth became the dominant process.

The different capabilities of lateral and vertical foreign-particle transport play a crucial role in driving the spatially non-uniform crystal growth process. The faster lateral growth indicates that the lateral transport of foreign particles is more effective in promoting crystal growth compared to vertical transport. However, as the grain boundaries begin to converge and touch, lateral diffusion is largely hindered, causing most foreign particles to become trapped at the grain boundaries. Consequently, the crystal expels the remaining foreign particles to the upper free solid–liquid interface, allowing growth to proceed predominantly in the vertical direction.

The kinetic pathway of the MR mode

In the MR mode, local melting events were observed to correlate with a distinct bay-like growth-front morphology. As illustrated in Fig. 3a, the large grain initially had a bay-like shape, characterized by a peak near the edges of its horizontal projection (t = 7.36 h). However, as the bay-like crystal grew, a substantial portion of its low-lying region melted (t = 7.61 h), leaving behind a considerable number of foreign particles in the melted area. Subsequently, recrystallization occurred, and the crystal grew with a slightly altered morphology compared to its state before melting (t = 11.04 h).

To understand how the bay-like crystal morphology impacted local melting and recrystallization events, we tracked the evolution of the number of foreign particles (N_s) and the average order parameter ($\langle \overline{q_6} \rangle$) near the melting growth front (see Methods for the calculation details). Before melting, N_s increased whereas $\langle \overline{q_6} \rangle$ decreased above the region about to melt (Fig. 3b), indicating that foreign particles progressively diffused towards the front of the impending melting region. During melting, foreign particles above the low-lying area diffused into the melting region, increasing their number density within that region. Simultaneously, a transient nucleus formed above the melting region, resulting in a temporary increase in $\langle \overline{q_6} \rangle$.

The melting and recrystallization of grains occurred in both the lateral and vertical directions simultaneously. As shown in Fig. 3c, the crystals initially exhibited a faster lateral growth compared to their vertical growth. Figure 3d illustrates the $\Delta N^{\perp}_{\mathrm{solid}}$ distribution on the x–y plane and the $\Delta N^{\parallel}_{\mathrm{solid}}$ distribution at a height near the growth front. During melting, the crystal size decreased in the both lateral and vertical directions, which was accompanied by a retreat of the growth front in the low-lying areas. The region around the peak remained relatively stable. Upon recrystallization, the retreating growth front re-advanced, resulting in crystal expansion in both the lateral and vertical directions.

Summarizing these observed behaviours, we conclude that the specific pathway of foreign-particle transportation plays a critical role in triggering local melting events. In the bay-like crystal morphology, there exist both a 'fast-growing area' (regions around the peak) and a 'lagged-growing area' (low-lying regions). During crystal growth, the fast-growing area 'pushes' foreign particles laterally towards the region above the lagged-growing area, resulting in their accumulation. This accumulation shifts the melting line and increases frustration at the growth front, ultimately triggering the melting of the slower-growing area (Supplementary Video 2). After melting, foreign particles at the crystal interface gradually diffuse away, facilitating the recrystallization of the original crystalline domains. Extended Data Fig. 3 illustrates the 3D microstructural evolution of the melting region. In subsequent crystal growth processes, recurring melting and recrystallization events can happen again as the crystal retains a bay-like morphology.

The delicate local balance between crystallization and melting, modulated by the concentration of foreign particles at the growth front, is key to the emergence of the dynamic MR mode. More precisely, melting is driven by a local decrease in the melting point due to the enrichment of foreign particles on the liquid side of the growth front, which destabilizes the crystal surface. When local quasi-equilibrium is achieved, melting ceases. This pause in crystal growth allows time for the accumulated foreign particles to diffuse away, thus increasing the local melting point and enabling crystal growth to resume. This process repeats periodically, giving rise to the MR mode.

The frequency peaks of the MR mode occur near the crystal–glass transition boundary (Fig. 1a), as both are linked to the thermodynamic stability limit of the crystal. The liquid phase coexisting with high-density crystals remains mobile because its local volume fraction is lower than that of the glass-forming regime. However, the particle dynamics are slow enough to allow the development of long-lived, inhomogeneous distributions of foreign particles, which are crucial for the activation of the MR mode.

This scenario is supported by our measurements of the α relaxation time τ_α of the supercooled liquid before crystallization, which ranged from 0.15 to 0.25 h. During melting, we observed enhanced particle mobility above the growth front, particularly in the largest particles. These findings indicate a dynamical influence on crystallization, potentially linking melting and recrystallization to vitrification. However, as direct measurements of slow relaxation remain limited, definitive proof awaits further investigation.

Additionally, we observed avalanche-like crystallization deep within the glass phase in our system (indicated by the L in Fig. 1a, the phase diagram with foreign particles). In this regime, strong structural frustration limited the crystal size within experimental timescales. In hard-sphere glass systems, avalanche crystallization[29,52] has been shown to be triggered by the stochastic instability of the force network formed in a glass state, which proceeds through the resulting particle mobility[30]. Crystallization in liquids is thermodynamically driven, whereas in glasses it is primarily governed by mechanical factors.

Grain size and growth-front morphology

Based on the above findings, it is clear that grain size and growth-front morphology are crucial elements that impact crystal growth in systems with foreign particles. In this section, we introduce two quantitative parameters, the average grain size (L) and the skewness of the crystal landscape (skew), to characterize how these two factors influence crystal growth.

We measured the probability distribution of the local heights of a grain $p(h)$ and calculated the skewness as the third-order moment of $p(h)$ (see Methods for the calculation details). The relation between $p(h)$ and h/d is shown in Fig. 4a. A peak in the distribution at low h indicates that the lagged-growing area predominates over the fast-growing

https://doi.org/10.1038/s41567-025-02870-4

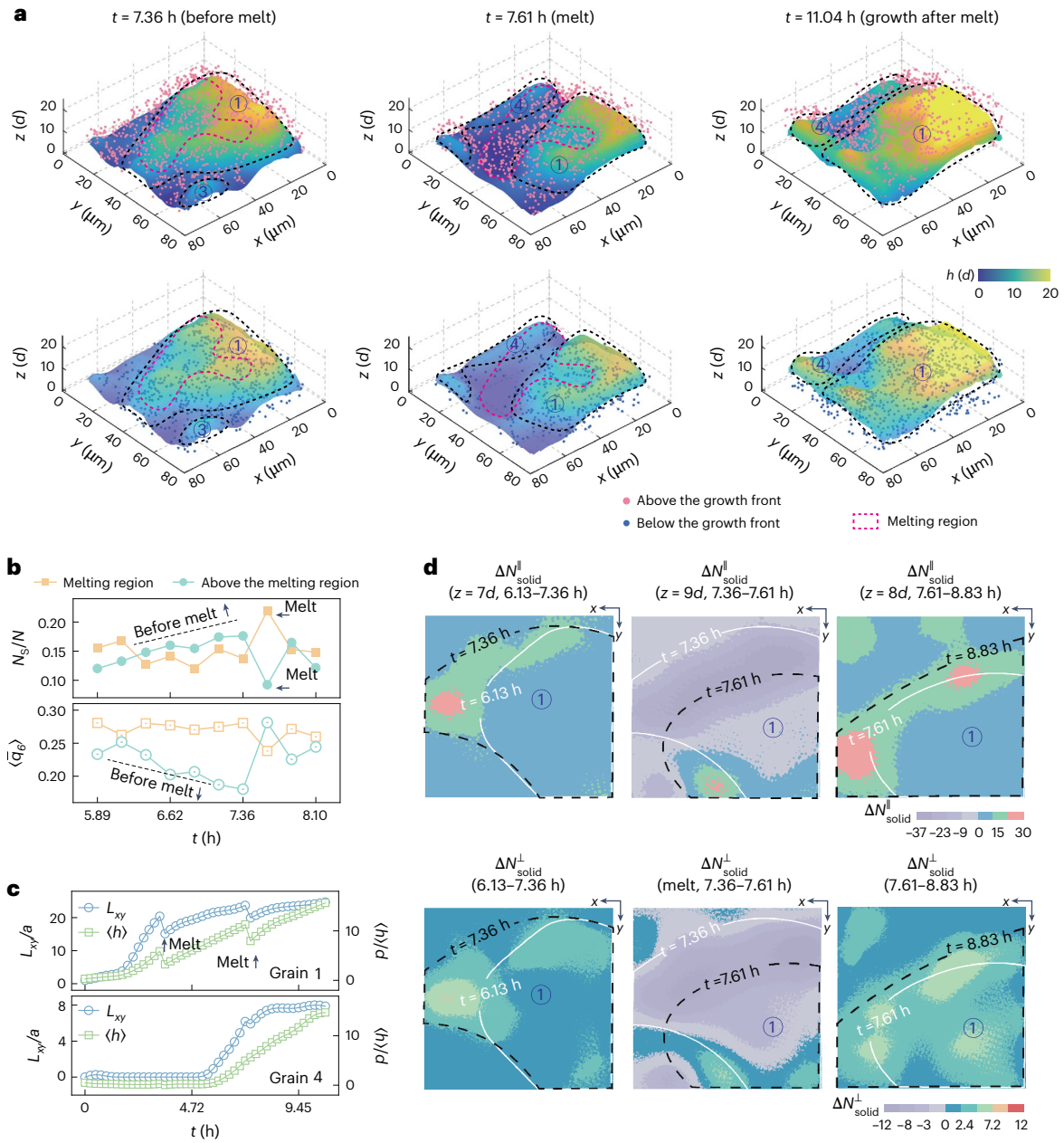

Fig. 3 | Kinetic pathways of the MR growth mode. a, Evolution of the growth-front morphology and foreign-particle distribution. Top, foreign particles (pink spheres) within the four layers above the growth front. Bottom, their distribution (blue spheres) within the grain. The colour bar represents the local height of the solid. The melting region is outlined by a magenta dotted line. **b**, Temporal evolution of the foreign-particle fraction (N_s/N, top) and the average bond orientation order ($\langle\overline{q_6}\rangle$, bottom) in both the melting region and the area above it, showing changes around the melting event. **c**, Temporal evolution of grain size in the lateral direction (L_{xy}) and vertical direction ($\langle h\rangle$). **d**, Temporal evolution of the local change in the number of solid particles $\Delta N^{\parallel}_{\mathrm{solid}}(x, y, z)$ at a fixed height z and its integration along the z axis, $\Delta N^{\perp}_{\mathrm{solid}}(x, y)$. The white and black dashed lines denote the initial and final positions of the growth front over the observed time.

area, resulting in a positive skewness (>0). By contrast, a peak at high h indicates that the fast-growing area is catching up and occupying a substantial portion of the region, which corresponds to a negative skewness (<0). The bimodal distribution implies that the fast-growing and lagged-growing areas are competing, leading to skewness close to zero (-0), which is characteristic of a bay-like growth morphology of the growth front, as depicted in Fig. 4a.

In the parameter space of L and skew (Fig. 4b), the two growth modes follow distinct patterns. For the CG mode, as the grain size increased, the skewness transitioned from positive to negative, with the crystal growing stably and the high-h area increasing, as illustrated in Fig. 4a. This stability was facilitated by cooperation between the fast-growing and lagged-growing areas, which allowed foreign particles to be laterally transported to the grain boundaries, thus promoting stable growth. In the MR mode, when the grains were small, the skewness was positive, as the lagged-growing area predominated. Foreign particles were laterally transported to the surrounding liquid area and vertically to the front, ensuring stable growth. As the grain size increased and the growth front developed a bay-like morphology, the skewness decreased, becoming negative or approaching zero, as shown in Fig. 4a. In this scenario, the fast-growing area competed with the lagged-growing area, leading to an accumulation of foreign particles at the front of the lagged-growing area, which caused crystal melting. Upon melting, the skewness became positive again (Fig. 4a)

https://doi.org/10.1038/s41567-025-02870-4

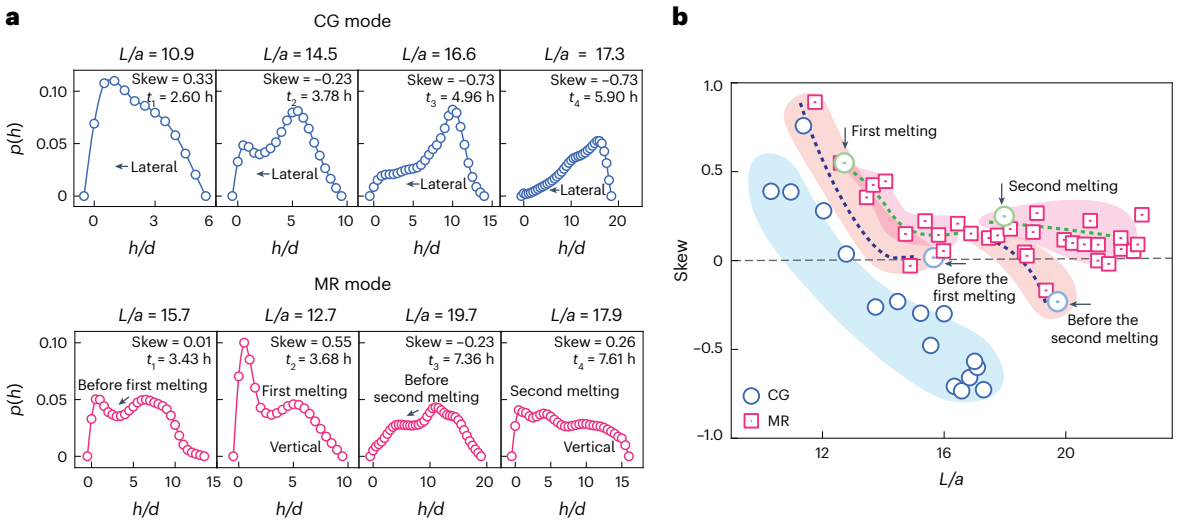

Fig. 4 | Grain size and growth-front morphology for the two growth modes. **a**, Temporal evolution of the probability distribution of the local heights of a single grain. Arrows indicate the directional flow of foreign-particle transport. **b**, Crystal morphology as a function of the skewness of the solid height probability distribution (skew) and the average grain size (L). The plot highlights distinct trends for the CG and MR modes.

as the high-h area shrank. The foreign particles were then transported to the surrounding lagged-growing area, facilitating recrystallization.

In the CG mode, the synergy between the rapidly growing area and the residual liquid zone is essential. This cooperation balances the lateral and vertical transport of foreign particles, allowing the crystal to grow stably. In contrast, the MR mode involves competition between the fast-growing and lagged-growing areas. When the concentration of foreign particles at the front of the lagged-growing region exceeds a threshold, the crystal melts, thereby resetting the growth dynamics.

Summary and outlook

In addition to the expected CG mode, our study uncovered a distinct MR growth mode during the crystallization process in systems containing foreign particles. We found that grain size and growth-front morphology play a critical role in shaping the crystallization dynamics by modulating the transport behaviour of foreign particles. In the CG mode, which is characterized by a relatively small critical grain size and high nuclei density, the growth front exhibits a rugged landscape with peaks representing crystalline regions and valleys of liquid phases. Foreign particles are effectively transported laterally to grain boundaries and vertically to the upper liquid regions, promoting uninterrupted, continuous grain growth.

By contrast, the MR mode is associated with a larger critical grain size and lower nuclei density, so that the competition between fast-growing and lagged-growing areas becomes more pronounced. The growth of fast-growing regions drives the lateral and vertical transport of foreign particles towards the lagged-growing areas. In large grains, where the growth front adopts a bay-like morphology, the accumulation of foreign particles at the lagged-growing front increases over time. When the particle concentration reaches a critical threshold, the excess frustration at the interface triggers localized melting of the crystal growth front. This melting event allows for the redistribution of foreign particles, ultimately facilitating recrystallization and modifying the crystal morphology. Thus, the interplay between foreign-particle transport and growth-front morphology governs the dynamic transitions between CG and the MR mechanism.

In our experimental set-up, the spatial distribution of foreign particles substantially influences the initial configuration of the crystal growth trajectory, as illustrated in Extended Data Fig. 1c. In the CG mode, a relatively uniform distribution of foreign particles during nucleation results in a high density of initial nuclei, leading to smaller grain sizes. This configuration enhances the capacity of grain boundaries to trap foreign particles, thus allowing effective lateral and vertical transport. The rugged morphology of the growth front further facilitates the continuous and steady expansion of the crystal structure.

By contrast, the MR mode arises from a non-uniform spatial distribution of foreign particles, leading to a lower nucleation density and larger grains. The reduced availability of grain boundaries limits the capacity of the system to trap foreign particles in these regions. As grain growth proceeds, the bay-like morphology of the growth front causes foreign particles to accumulate unevenly, particularly at lagged-growing regions, ultimately triggering localized melting. Recrystallization follows as the system redistributes foreign particles, which allows the crystal to stabilize and grow in a modified configuration.

Unveiling the relation between initial crystal configurations and their dynamic pathways provides valuable insights into predicting the evolution of crystal growth trajectories and determining the final crystalline morphologies. This understanding may enable better control over material properties by manipulating nucleation conditions and foreign-particle distributions.

Here we consider the influence of the interaction range of a potential on the crystal growth mode. We infer that the MR mode is less probable in hard-sphere and short-range attractive systems[29,53,54] compared to long-range systems. This is because the crystal–liquid free energy difference is considerably larger in short-range systems than in long-range systems, resulting in weaker impurity-induced melting-point depression effects in the former.

To replicate MR modes in theoretical models, it is essential to incorporate interactions between foreign particles and the advancing crystal growth front. Additionally, the dynamics of the supercooled liquid must be taken into account. Considering these effects would allow for a more accurate representation of the complex interplay between crystal growth, melting and impurity-particle diffusion. Developing a quantitative theoretical framework that captures these critical features remains a key challenge for future research.

The observed MR mode holds great potential for advanced impurity purification and grain microstructural control. Traditional purification methods, such as fractional crystallization, often suffer from inefficiencies and loss of valuable components[55]. Similarly, zone-refining techniques require precise control of heating rates when purifying crystals because they exploit concentration differences

of impurities in the solid and liquid phases[56]. By contrast, the MR growth mechanism offers a new potential strategy for producing large high-purity crystals. By manipulating the initial configuration, such as by tuning the substrate properties to induce the formation of large nuclei, several cycles of melting and recrystallization can reduce the impurity content. This iterative purification process, driven by dynamic adjustments of the grain size and growth-front morphology, enhances the efficiency of impurity expulsion while maintaining crystal integrity.

Our findings also offer valuable insights into controlling grain microstructure, a critical determinant of material performance in alloy manufacturing. Grain refinement enhances yield strength, hardness, toughness and other mechanical properties by reducing the grain size, as noted in foundational studies on nanocrystalline materials[57]. Our study demonstrates that targeted grain-size control can be achieved using straightforward techniques, such as varying the spatial distribution of foreign particles or adjusting the crystallization rate. When crystallization rates are high or foreign particles are uniformly distributed in the substrate, the nucleation density increases, producing smaller grains. In this scenario, foreign particles accumulate at grain boundaries, exerting a pinning effect that hinders grain growth, leading to grain refinement. Conversely, slower crystallization rates or non-uniform foreign-particle distributions result in lower nucleation densities and larger grains. The melting process selectively eliminates smaller grains through localized melting, promoting the growth of larger grains through repeated cycles of recrystallization. These findings open pathways for optimizing the grain structure to enhance mechanical properties and for developing more efficient, scalable purification techniques by leveraging controlled dynamic crystallization processes.

Online content

Any methods, additional references, Nature Portfolio reporting summaries, source data, extended data, supplementary information, acknowledgements, peer review information; details of author contributions and competing interests; and statements of data and code availability are available at https://doi.org/10.1038/s41567-025-02870-4.

References

1. Myerson, A. *Handbook of Industrial Crystallization* (Butterworth-Heinemann, 2002).
2. Chen, Q., Bae, S. C. & Granick, S. Directed self-assembly of a colloidal kagome lattice. *Nature* **469**, 381–384 (2011).
3. Damasceno, P. F., Engel, M. & Glotzer, S. C. Predictive self-assembly of polyhedra into complex structures. *Science* **337**, 453–457 (2012).
4. Gasser, U., Weeks, E. R., Schofield, A., Pusey, P. & Weitz, D. Real-space imaging of nucleation and growth in colloidal crystallization. *Science* **292**, 258–262 (2001).
5. Pusey, P. N. & Van Megen, W. Phase behaviour of concentrated suspensions of nearly hard colloidal spheres. *Nature* **320**, 340–342 (1986).
6. Zhu, J. et al. Crystallization of hard-sphere colloids in microgravity. *Nature* **387**, 883–885 (1997).
7. Wang, H. et al. Freezing shrinkage dynamics and surface dendritic growth of floating refractory alloy droplets in outer space. *Adv. Mater.* **36**, 2313162 (2024).
8. Wolde, P. R. T. & Frenkel, D. Enhancement of protein crystal nucleation by critical density fluctuations. *Science* **277**, 1975–1978 (1997).
9. Tan, P., Xu, N. & Xu, L. Visualizing kinetic pathways of homogeneous nucleation in colloidal crystallization. *Nat. Phys.* **10**, 73–79 (2014).
10. Kawasaki, T. & Tanaka, H. Formation of a crystal nucleus from liquid. *Proc. Natl Acad. Sci. USA* **107**, 14036–14041 (2010).
11. Li, M. et al. Revealing thermally-activated nucleation pathways of diffusionless solid-to-solid transition. *Nat. Commun.* **12**, 4042 (2021).
12. Wang, Z., Wang, F., Peng, Y., Zheng, Z. & Han, Y. Imaging the homogeneous nucleation during the melting of superheated colloidal crystals. *Science* **338**, 87–90 (2012).
13. Peng, Y. et al. Two-step nucleation mechanism in solid–solid phase transitions. *Nat. Mater.* **14**, 101–108 (2015).
14. Li, M., Chen, Y., Tanaka, H. & Tan, P. Revealing roles of competing local structural orderings in crystallization of polymorphic systems. *Sci. Adv.* **6**, eaaw8938 (2020).
15. Arai, S. & Tanaka, H. Surface-assisted single-crystal formation of charged colloids. *Nat. Phys.* **13**, 503–509 (2017).
16. Chen, Y. et al. Visualizing slow internal relaxations in a two-dimensional glassy system. *Nat. Phys.* **19**, 969–977 (2023).
17. Meng, G., Paulose, J., Nelson, D. R. & Manoharan, V. N. Elastic instability of a crystal growing on a curved surface. *Science* **343**, 634–637 (2014).
18. Chen, Y. et al. Morphology selection kinetics of crystallization in a sphere. *Nat. Phys.* **17**, 121–127 (2021).
19. Irvine, W. T., Vitelli, V. & Chaikin, P. M. Pleats in crystals on curved surfaces. *Nature* **468**, 947–951 (2010).
20. Hwang, H., Weitz, D. A. & Spaepen, F. Direct observation of crystallization and melting with colloids. *Proc. Natl Acad. Sci. USA* **116**, 1180–1184 (2019).
21. Tegze, G. et al. Diffusion-controlled anisotropic growth of stable and metastable crystal polymorphs in the phase-field crystal model. *Phys. Rev. Lett.* **103**, 035702 (2009).
22. Freitas, R. & Reed, E. J. Uncovering the effects of interface-induced ordering of liquid on crystal growth using machine learning. *Nat. Commun.* **11**, 3260 (2020).
23. Mullins, W. W. & Sekerka, R. Stability of a planar interface during solidification of a dilute binary alloy. *J. Appl. Phys.* **35**, 444–451 (1964).
24. Warren, J. A. & Langer, J. Prediction of dendritic spacings in a directional-solidification experiment. *Phys. Rev. E* **47**, 2702 (1993).
25. Langer, J. S. Instabilities and pattern formation in crystal growth. *Rev. Mod. Phys.* **52**, 1 (1980).
26. Losert, W., Shi, B. & Cummins, H. Evolution of dendritic patterns during alloy solidification: onset of the initial instability. *Proc. Natl Acad. Sci. USA* **95**, 431–438 (1998).
27. Gránásy, L., Pusztai, T., Tegze, G., Warren, J. A. & Douglas, J. F. Growth and form of spherulites. *Phys. Rev. E* **72**, 011605 (2005).
28. Watanabe, K., Kawasaki, T. & Tanaka, H. Structural origin of enhanced slow dynamics near a wall in glass-forming systems. *Nat. Mater.* **10**, 512–520 (2011).
29. Zaccarelli, E. et al. Crystallization of hard-sphere glasses. *Phys. Rev. Lett.* **103**, 135704 (2009).
30. Yanagishima, T., Russo, J. & Tanaka, H. Common mechanism of thermodynamic and mechanical origin for ageing and crystallization of glasses. *Nat. Commun.* **8**, 15954 (2017).
31. Gao, Q. et al. Fast crystal growth at ultra-low temperatures. *Nat. Mater.* **20**, 1431–1439 (2021).
32. Cacciuto, A., Auer, S. & Frenkel, D. Onset of heterogeneous crystal nucleation in colloidal suspensions. *Nature* **428**, 404–406 (2004).
33. De Villeneuve, V. W. et al. Colloidal hard-sphere crystal growth frustrated by large spherical impurities. *Science* **309**, 1231–1233 (2005).
34. Allahyarov, E., Sandomirski, K., Egelhaaf, S. U. & Löwen, H. Crystallization seeds favour crystallization only during initial growth. *Nat. Commun.* **6**, 7110 (2015).
35. Farmanesh, S. et al. Specificity of growth inhibitors and their cooperative effects in calcium oxalate monohydrate crystallization. *J. Am. Chem. Soc.* **136**, 367–376 (2014).
36. Schmidt, C. & Ulrich, J. Morphology prediction of crystals grown in the presence of impurities and solvents—an evaluation of the state of the art. *J. Cryst. Growth* **353**, 168–173 (2012).

37. Kuvadia, Z. B. & Doherty, M. F. Effect of structurally similar additives on crystal habit of organic molecular crystals at low supersaturation. *Cryst. Growth Des.* **13**, 1412–1428 (2013).
38. Zhao, M., Xiong, Y., Shang, Y. & Xu, X. Effect of nano-impurity on liquid/solid phase transition of water droplet. *J. Mol. Liq.* **398**, 124232 (2024).
39. Shklovskii, B. I. & Efros, A. L. *Electronic Properties of Doped Semiconductors*, Vol. 45 (Springer, 2013).
40. Erwin, S. C. et al. Doping semiconductor nanocrystals. *Nature* **436**, 91–94 (2005).
41. Zhao, J. et al. Structural and magnetic phase diagram of $CeFeAsO_{1-x}F_x$ and its relation to high-temperature superconductivity. *Nat. Mater.* **7**, 953–959 (2008).
42. Pramanik, S., Cherusseri, J., Baban, N. S., Sowntharya, L. & Kar, K. K. *Metal Matrix Composites: Theory, Techniques, and Applications* (Springer, 2017).
43. Zhang, S., Wang, Z., Guo, B. & Xu, J. Secondary nucleation in polymer crystallization: a kinetic view. *Polym. Cryst.* **4**, e10173 (2021).
44. Cabrera, N. & Vermilyea, D. in *Growth and Perfection of Crystals* (eds Doremus, R. H. et al.) 393–410 (Wiley, 1958).
45. Granasy, L. et al. Growth of 'dizzy dendrites' in a random field of foreign particles. *Nat. Mater.* **2**, 92–96 (2003).
46. Gránásy, L., Pusztai, T., Börzsönyi, T., Warren, J. A. & Douglas, J. F. A general mechanism of polycrystalline growth. *Nat. Mater.* **3**, 645–650 (2004).
47. Warren, J. A., Pusztai, T., Környei, L. & Gránásy, L. Phase field approach to heterogeneous crystal nucleation in alloys. *Phys. Rev. B* **79**, 014204 (2009).
48. Sangwal, K. Effects of impurities on crystal growth processes. *Prog. Cryst. Growth Characteriz. Mater.* **32**, 3–43 (1996).
49. Kubota, N. Effect of impurities on the growth kinetics of crystals. *Cryst. Res. Technol.* **36**, 749–769 (2001).
50. Stipp, A. & Palberg, T. Crystal growth kinetics in binary mixtures of model charged sphere colloids. *Philos. Mag.* **87**, 899–908 (2007).
51. Steinhardt, P. J., Nelson, D. R. & Ronchetti, M. Bond-orientational order in liquids and glasses. *Phys. Rev. B* **28**, 784 (1983).
52. Sanz, E. et al. Avalanches mediate crystallization in a hard-sphere glass. *Proc. Natl Acad. Sci. USA* **111**, 75–80 (2014).
53. Yunker, P., Zhang, Z., Aptowicz, K. B. & Yodh, A. G. Irreversible rearrangements, correlated domains, and local structure in aging glasses. *Phys. Rev. Lett.* **103**, 115701 (2009).
54. Ganapathi, D., Chakrabarti, D., Sood, A. & Ganapathy, R. Structure determines where crystallization occurs in a soft colloidal glass. *Nat. Phys.* **17**, 114–120 (2021).
55. Cabane, B. et al. Hiding in plain view: colloidal self-assembly from polydisperse populations. *Phys. Rev. Lett.* **116**, 208001 (2016).
56. Shinohara, M. et al. Recrystallization and zone melting of charged colloids by thermally induced crystallization. *Langmuir* **29**, 9668–9676 (2013).
57. Schiøtz, J., Di Tolla, F. D. & Jacobsen, K. W. Softening of nanocrystalline metals at very small grain sizes. *Nature* **391**, 561–563 (1998).

Methods

Experiments

We used a binary colloidal system comprising colloidal particles fluorescently dyed with nitrobenzoxadiazole and grafted with poly-hydroxystearic acid polymer. The particles had diameters of either 2.10 or 1.06 μm, with polydispersity ~2.5%. These particles were suspended individually in a non-polar solvent mixture of hexachloro-1,3-butadiene, tetrachloroethylene and decahydronaphthalene, with the concentrations adjusted to match the density and refractive index of the colloidal particles. Two suspensions with equal volume fractions were prepared and mixed at volumetric ratios ranging from 25:1 to 70:1.

To introduce charges, AOT (a surfactant) was added to the suspension. We also tested tetrabutylammonium bromide in a mixture of cyclohexyl bromide and cis-decalin to control electrostatic interactions. Although both systems had similar phase diagrams and growth modes, cyclohexyl bromide tended to decompose under prolonged laser scanning during confocal microscopy, releasing excess Br^- ions. This ionic flow increased the Debye length κ^{-1}, especially at low ionic strengths. Therefore, we primarily used the AOT system during imaging because of its greater stability.

The charged poly(methyl methacrylate) particles interacted through a weakly screened Coulomb repulsive potential: $u(r) = \alpha \exp(-\kappa\sigma(r/\sigma - 1))/(r/\sigma)$, where α is the effective interaction strength, σ is the particle radius and κ^{-1} is the Debye length. Here, $\kappa = \sqrt{4\pi\lambda_B n_{ion}}$, with $\lambda_B = e^2/4\pi\varepsilon\varepsilon_0 k_B T$ representing the Bjerrum length for monovalent ions, and where e is the elementary charge, ε the relative dielectric constant of the solvent, ε_0 the vacuum permittivity, k_B the Boltzmann constant and n_{ion} the ion number density. n_{ion} was estimated from the conductivity of the suspension through Walden's rule[58], which relates the conductivity to the ion mobility in the solvent as $\sigma_s = e^2 n_{ion} k_B T/(6\pi\eta\alpha_h)$, where η is the viscosity and α_h is the hydrodynamic radius of a micelle. Increasing the AOT concentration enhanced the conductivity and modified the screening length[59].

The suspension and the nickel powder were sealed between a cover glass, spacers and a slide glass to form a 100-μm cubic cell. Initial crystal formation was driven by capillary forces, followed by crystal melting induced by shearing with a magnet. Confocal microscopy, covering a field of 77 μm × 77 μm × 80–85 μm with 40-s stack capture times, was used to observe nucleation and growth processes.

In regions where both MR and CG modes coexist, we conducted about 30 independent experiments, observing a CG:MR event ratio of approximately 7:3, with 10% variability across conditions. Each extra condition was tested two to three times. Deep within the glass phase, only rare avalanche-like crystallization events were observed. The volume fraction error was 1–2%, and small particle concentration errors were 2–3%.

Bond orientational order and structural analysis

To distinguish local structure, we employed the bond orientational order parameter, second-order rotational invariants $\overline{q_l}$ and third-order rotational invariants $\overline{w_l}$ (refs. 51,60,61). The local bond orientational function is defined as $q_{l,m} = \sum_{f\in F(i)} \frac{A(f)}{A} Y_{l,m}(\theta_{ij}, \phi_{ij})$, where A is the total surface area of the Voronoi cell boundary, $A(f)$ is the surface area of the Voronoi cell facet F and $Y_{l,m}(\theta_{ij}, \phi_{ij})$ is the spherical harmonics with $m \in [-l, l]$. The value of l reflects different symmetries, and θ_{ij} and ϕ_{ij} are the polar and azimuthal angles of the vector $\mathbf{r}_{ij} = \mathbf{r}_i - \mathbf{r}_j$, where $\mathbf{r}_i$ is the vector of central particle i and $\mathbf{r}_j$ is the vector of its neighbouring particle j.

To reduce thermal fluctuations, we introduced a coarse-graining version, defined as $Q_{l,m} = \frac{1}{N_b}\sum_{k=0}^{N_b} q_{l,m}(k)$, where N_b represents the number of neighbouring particles identified through Delaunay triangulation. Subsequently, $\overline{q_l}$ and $\overline{w_l}$ are defined as follows:

$$\overline{q_l}(i) = \left(\frac{4\pi}{2l+1}\sum_{m=-l}^{l}|Q_{l,m}(i)|^2\right)^{1/2},$$

$$\overline{w_l}(i) = \sum_{m_1+m_2+m_3=0}^{l}\begin{pmatrix} l & l & l \\ m_1 & m_2 & m_3\end{pmatrix}\frac{Q_{l,m_1}(i)\,Q_{l,m_2}(i)\,Q_{l,m_3}(i)}{\left(\sum_{m=-l}^{l}|Q_{l,m}(i)|^2\right)^{3/2}},$$

where the term in parentheses represents the Wigner 3j symbol, which is non-zero only for $m_1 + m_2 + m_3 = 0$. This approach captures the symmetry information of local particle arrangements while minimizing thermal distortion.

Crystal size determination based on solid particle distribution

Particles with $\overline{q_6} > 0.3$ were classified as solid particles. To monitor the evolution of the crystal morphology, we calculated the local change in the number of solid particles $\Delta N^{\parallel}_{solid}(x,y,z)$ over a specific time period. The solid particle count, $N^{\parallel}_{solid}(x,y,z)$, represents the total number of solid particles within a cylindrical volume of radius $3a$ and height d centred at (x,y,z). Here, a is the interparticle spacing within the solid and d is the interlayer spacing of the (100) face in the formed BCC crystal lattice. Similarly, $\Delta N^{\perp}_{solid}(x,y)$ quantifies the change in the number of solid particles within an infinitely tall cylindrical volume of radius $3a$ centred at (x,y). The local height h of the crystal at (x,y) was then calculated as $h \equiv N^{\perp}_{solid}(x,y)d/N^{0}_{solid}$, where N^{0}_{solid} represents the average number of solid particles in a standard crystal lattice within a cylindrical volume of radius $3a$ and height d. This method provides a detailed way of tracking crystal growth and morphology evolution over time.

To compare the grain size in the two growth modes and illustrate the spatial non-uniformity of growth, we defined three metrics: the average grain size L, the grain size in the lateral direction L_{xy} and the characteristic height $\langle h\rangle$. The average grain size $L \equiv \sqrt[3]{N_{solid}}a$, where N_{solid} is the total number of solid particles within a grain and a is the interparticle spacing of the corresponding lattice structure. The growth speed of the crystal in Fig. 1a (bottom) was estimated as $\Delta L/\Delta t$. Owing to the anisotropic grain shape, the grain size in the lateral direction was defined as $L_{xy} \equiv \sqrt{N^{max}_{xy}}a$, where N^{max}_{xy} is the number of solid particles within the layer of the crystal with the largest projected area in the x–y direction. The characteristic height $\langle h\rangle$ was defined as $\langle h\rangle = N_{solid}d/\langle N_{xy}\rangle$, where $\langle N_{xy}\rangle$ represents the average number of particles per layer. These metrics provide a comprehensive understanding of the grain size and growth dynamics in both growth modes.

Identification of the locally melted region

The entire space was divided into numerous small cubes (4 μm × 4 μm × 5 μm). Local melting events were identified by monitoring the change in the solid fraction within each cube. Each cube was assigned a unique ID, which allowed us to track the morphological evolution of the crystal by following the changes associated with these cube IDs. We selected the solid region at the moment before melting (t = 7.36 h) and calculated the change in $\langle\overline{q_6}\rangle$ for this solid region when melting occurred (t = 7.61 h). The region where $|\Delta q_6| > 0.1$ was identified as the melting region. In Fig. 3b, the region within 4d above the upper interface of the melting region was identified as 'above the melting region'. Extended Data Fig. 3 shows the evolution of the 3D structure of the melting region over time.

Definition of skewness

We quantified the morphology of the growth front using the skewness of the probability distribution of the solid height. The skewness parameter describes the asymmetry of the crystal height distribution and is defined as $\text{skew} = \frac{n}{(n-1)(n-2)}\sum_{i=1}^{n}\left(\frac{h_i - \langle h\rangle}{s}\right)^3$, where the crystal height h at (x,y) was calculated as $h_i \equiv N^{\perp}_{solid}(x,y)d/N^{0}_{solid}$, with $N^{\perp}_{solid}(x,y)$ representing the number of solid particles within an infinitely tall cylindrical volume of radius $3a$ centred at (x,y). N^{0}_{solid} is the average number of solid particles in a standard crystal lattice within a cylindrical volume of radius $3a$ (where a is the interparticle spacing) and

height d (the interlayer distance). The total number of columns is denoted as n, $\langle h \rangle$ is the average height over all columns and the standard deviation of the crystal height is given by $s \equiv \sqrt{\sum_{i=1}^{n} (h_i - \langle h \rangle)^2 / n}$. A skewness of 0 indicates a normal distribution, positive values indicate a right-handed tail and negative values indicate a left-handed tail. For bimodal distributions, the sign of the skewness depends on the relative heights and positions of the two peaks. For Fig. 4, we selected a grain and calculated the crystal heights at different locations in the x–y plane, using the resulting crystal height distribution to compute the skewness.

Uniformity of the distribution of foreign particles

We calculated the density variance of foreign particles $\langle \delta\rho^2 \rangle$ at the initial stage of nucleation, as commonly used in hyperuniformity analysis: $\langle \delta\rho^2 \rangle \equiv (\langle N_s^2 \rangle - \langle N_s \rangle^2)/R^3$ (ref. 62), where N_s is the number of foreign particles within many spherical volumes of radius R and $\langle \cdot \rangle$ denotes the ensemble average. As shown in Extended Data Fig. 1c, the density variance of foreign particles in the MR mode is higher than in the CG mode, indicating a greater non-uniformity in their spatial distribution.

Data availability

The data that support the findings of this study are available from the corresponding authors upon request. Source data are provided with this paper.

Code availability

The codes used in this study are available from the corresponding authors upon request.

References

58. Dalal, M. *A Textbook of Physical Chemistry*, Vol. 1 (Dalal Institute, 2018).
59. Hsu, M. F., Dufresne, E. R. & Weitz, D. A. Charge stabilization in nonpolar solvents. *Langmuir* **21**, 4881–4887 (2005).
60. Lechner, W. & Dellago, C. Accurate determination of crystal structures based on averaged local bond order parameters. *J. Chem. Phys.* **129**, 114707 (2008).
61. Mickel, W., Kapfer, S. C., Schröder-Turk, G. E. & Mecke, K. Shortcomings of the bond orientational order parameters for the analysis of disordered particulate matter. *J. Chem. Phys.* **138**, 044501, (2013).
62. Torquato, S. & Stillinger, F. H. Local density fluctuations, hyperuniformity, and order metrics. *Phys. Rev. E* **68**, 041113 (2003).

Acknowledgements

P.T. acknowledges support from the National Natural Science Foundation of China (Grant Nos. 12425503, 12174071 and 12035004), the Space Application System of China Manned Space Program (Grant No. KJZ-YY-NLT0501), the Innovation Program of Shanghai Municipal Education Commission (Grant No. 2023ZKZD06) and the Shanghai Pilot Program for Basic Research-FuDan University (Grant No. 22TQ003). Q.G. acknowledges support from the China Postdoc Science Foundation (Grant No. BX20220072). H.T. acknowledges support from a Grant-in-Aid for Specially Promoted Research (Grant No. JP20H05619) from the Japan Society for the Promotion of Science.

Author contributions

H.T. and P.T. conceived and supervised the research and wrote the paper. Q.G., D.X. and Y.C. performed the experiments. Q.G., H.F., D.X., Y.C., H.T. and P.T. analysed the data.

Competing interests

The authors declare no competing interests.

Additional information

Extended data is available for this paper at https://doi.org/10.1038/s41567-025-02870-4.

Supplementary information The online version contains supplementary material available at https://doi.org/10.1038/s41567-025-02870-4.

Correspondence and requests for materials should be addressed to Hajime Tanaka or Peng Tan.

Peer review information *Nature Physics* thanks Dora Izzo and the other, anonymous, reviewer(s) for their contribution to the peer review of this work.

https://doi.org/10.1038/s41567-025-02870-4

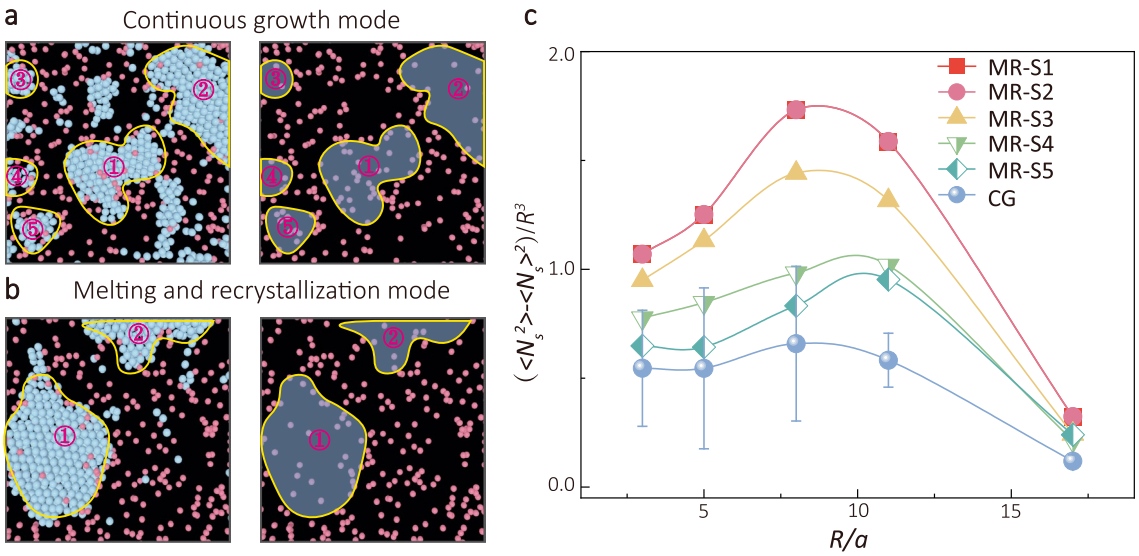

Extended Data Fig. 1 | Spatial distribution of foreign particles and nuclei at initial configuration. a,b, Initial distribution of nuclei and foreign particles for two growth modes. Foreign particles are labelled in pink. Left panels: Nuclei are shown in light blue. Right panels: Shaded areas represent the distribution of foreign particles within nuclei. **c**, Density variance $\langle \delta\rho^2 \rangle$ of foreign particles at the initial stage of nucleation for both growth modes. Five samples of MR growth modes and four samples of CG mode are analyzed. The CG mode curve represents the mean values of four measurements, with error bars indicating their upper and lower bounds.

https://doi.org/10.1038/s41567-025-02870-4

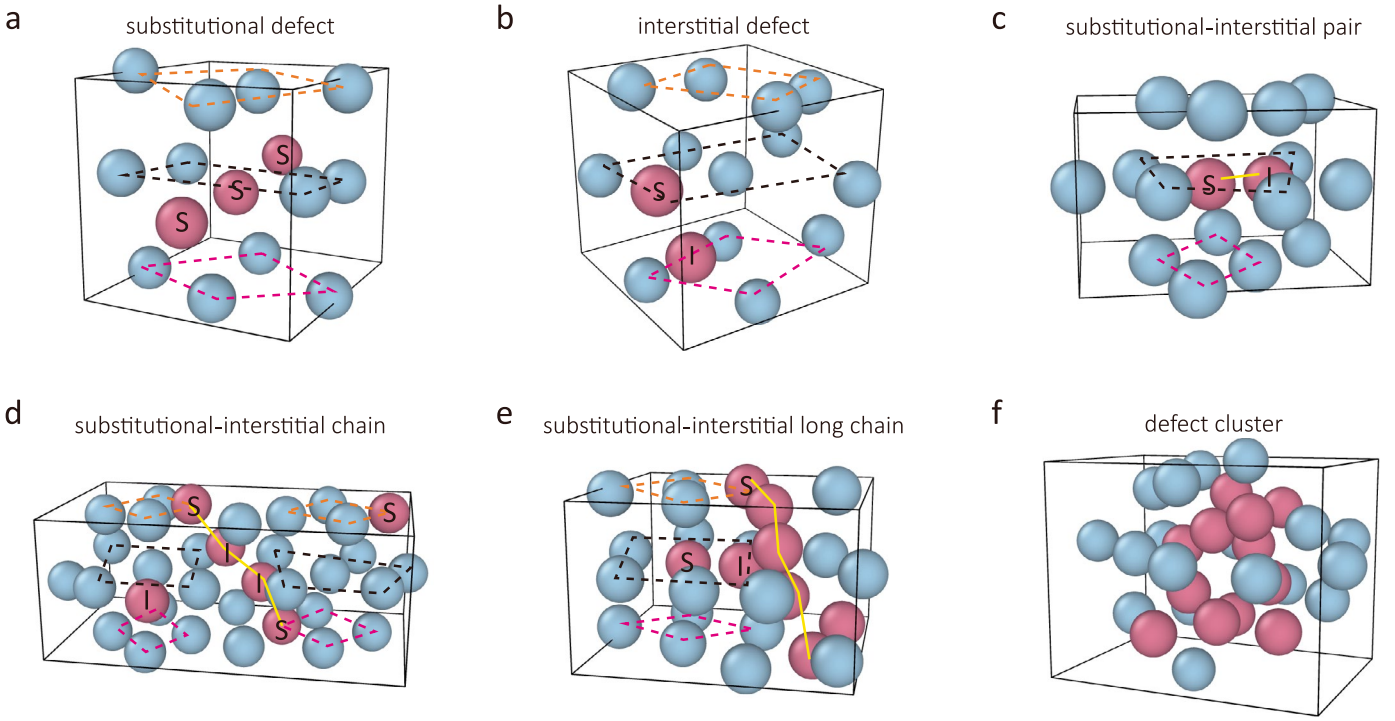

Extended Data Fig. 2 | Defect types of foreign particles in BCC lattice. **a**, Substitutional: A single foreign particle occupies a lattice site. **b**, Interstitial: A single foreign particle occupies an interstitial site. **c**, Substitutional interstitial pair: One foreign particle occupies a lattice site and the other an interstitial site. **d**,**e**, Defect chain: Substitutional-interstitial pairs form a defect chain, with crystal order decreasing as the number of foreign particles in the chain increases. **f**, Cluster: Foreign particles aggregate into a cluster, causing geometric frustration that impedes crystallization.

https://doi.org/10.1038/s41567-025-02870-4

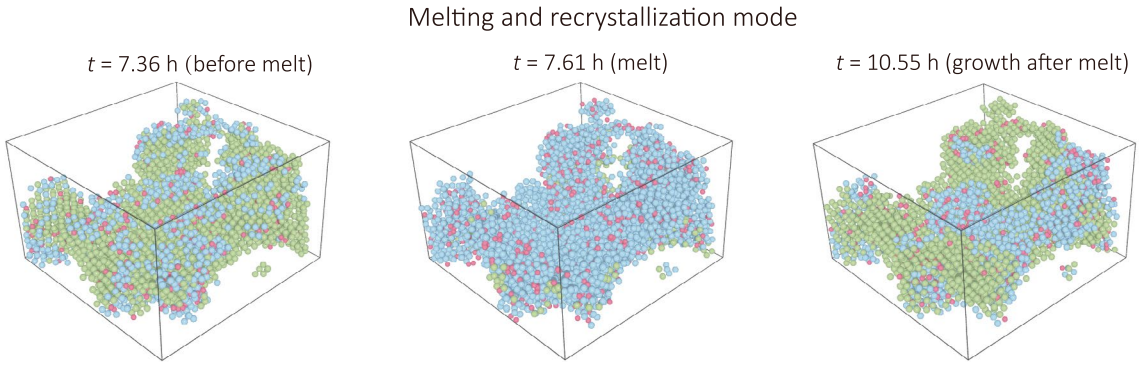

Extended Data Fig. 3 | 3D micro-structure of the melting region. Evolution of the 3D structure in the melting region before, during, and after melting, with solid particles in olive green, liquid particles in blue, and foreign particles in pink.